ACS OMEGA

http://pubs.acs.org/journal/acsodf

Article

An Inorganic Fluorescent Chemosensor: Rational Design and Selective Mg^{2+} Detection

Theodore Gerard, Yang Wei, Erwin Weerawardhana, Adriana Lugosan, Matthias Zeller, Diane A. Dickie, Pengfei Li,* and Wei-Tsung Lee*

Cite This: *ACS Omega* 2023, 8, 3835−3841

Read Online

ACCESS | Metrics & More | Article Recommendations | Supporting Information

ABSTRACT: A Zn^{2+} based complex, **3**, displays greatly increased fluorescence emission in the presence of Mg^{2+}. Fluorescent and computational studies suggest that **3** selectively interacts with Mg^{2+} due to optimal cavity size formation between two uncoordinated pyrazole side arms. This work thus represents a new approach to the development of fluorescent chemosensors.

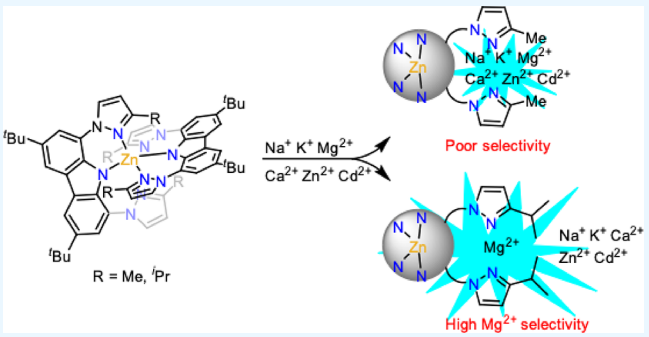

INTRODUCTION

The first fluorescent chemosensor was developed by Goppelsröder in 1867 for the detection of Al^{3+} ions.[1] Since then, fluorescent chemosensors have seen wide application in fields from analytical chemistry to physiology for the accurate measurements of various analytes in solution. An important area of fluorescent chemosensor application is in the detection of biologically relevant cations, which maintain vital functions for human health. Critical for these measurements is the ability of the sensor to respond with high selectively to the desired analyte. Because of this, researchers are still working on developing probes for a wide range of cations, while also looking into the fundamental factors affecting selectivity. While a range of methods for developing chemosensors exist, including the development of fluorescent MOF-based sensors,[2] the most common approach for cation detection is through the use of molecular sensors. This is especially true for sensors developed with the goal of studying *in vivo* analyte concentrations.

Most fluorescent chemosensors are developed using strictly organic motifs.[3−5] However, organic probes can adopt a limited number of geometries (commonly due to sp^2 and sp^3 hybridizations). Given the need for a highly conjugated fluorophore, many organic probes are required to be planar which, in turn, may limit selectivity.[3−6] Indeed, it is well known that, in proteins, 3D geometric parameters such as cavity shape and size may play a significant role in determining with which cation a given receptor best binds.[7] Given this, we were curious to see if inorganic complexes, which may readily adopt a number of geometries, may be used to create and fine tune binding site cavities in order to increase specificity for a biologically relevant cation. Surprisingly, an extensive review of the available literature suggests that cation sensors using a molecular inorganic scaffold are rare.[3−5,8] Thus, to study the fundamental benefits of using inorganic fluorescent chemosensors, we set out to design a fluorescent probe in which initial complexation to a metal center enhanced the ability to selectively detect a desired analyte. To our satisfaction, this concept worked well in the design of a sensor capable of highly selective interaction with Mg^{2+}. Notably, the magnesium ion is not only an important biological ion but is also known to be harder to detect using fluorescent chemosensors when in the presence of Ca^{2+}.[3,6−14] While designing the sensor, we were inspired by the zinc-finger protein motif, in which d^{10} zinc ions support protein folding,[15] and targeted zinc-based complexes with adjustable binding site cavities. Thus, we synthesized a series of novel homoleptic Zn^{2+} complexes supported by two NNN pincer ligands, $Cz^{tBu}(Pyr^{R})_2^-$ (R = H, Me, ^{i}Pr).[16] Further modifications are needed before the most successful sensor, **3**, is available for biological applications. Still, our results act as a "proof-of-concept" and support the need for further investigation of fluorescent chemosensors that take advantage of the fundamental benefits of using an inorganic approach toward sensor design.

Received: September 19, 2022
Accepted: November 16, 2022
Published: January 19, 2023

https://doi.org/10.1021/acsomega.2c06058
ACS Omega 2023, 8, 3835−3841

EXPERIMENTAL SECTION

Materials and Methods. All manipulations were performed under a nitrogen atmosphere using standard Schlenk techniques or in an M. Braun UNIlab Pro glovebox. Glassware was dried at 150 °C overnight. Acetonitrile, dichloromethane, diethyl ether, *n*-pentane, tetrahydrofuran, and toluene were purified using a Pure Process Technology solvent purification system. Before use, an aliquot of each solvent was tested with a drop of sodium benzophenone ketyl in THF solution. All reagents were purchased from commercial vendors and used as received. $HCz^{tBu}(Pyr^{H})_2$, $HCz^{tBu}(Pyr^{Me})_2$, and $HCz^{tBu}(Pyr^{iPr})_2$ were prepared according to a modified literature procedure.[15] ^1H NMR data were recorded on a Varian Inova 500 MHz spectrometer at 22 °C. Resonances in the ^1H NMR spectra are referenced to residual C_6D_5H at δ = 7.16 ppm. UV−visible spectra were recorded on an Agilent Cary 8454 UV−vis spectrophotometer equipped with a Unisoku Scientific Instruments Cryostat USP-203B for variable temperature experiments. Fluorescence emission spectra were recorded on a Shimadzu RF-6000 spectrofluorometer. Elemental analyses were conducted by Midwest Microlab, LLC (Indianapolis, IN).

General Synthesis of $(Cz^{tBu}(Pyr^{R})_2)_2Zn$ (R = H (1), Me (2), ^{i}Pr(3)). To a stirred solution of $HCz^{tBu}(Pyr^{R})_2$ (500 mg, 1.01−1.22 mmol) in THF (3 mL) at ambient temperature under a N_2 atmosphere was added a solution of lithium diisopropylamide (LDA) (1.06−1.28 mmol) in THF (2 mL) for 1 h. Solid $ZnCl_2$ (0.5−0.61 mmol) was added, and the resulting slurry was stirred for 12 h at ambient temperature. Volatiles were removed under reduced pressure, and the residue was extracted with toluene and filtered through Celite. The filtrate was dried *in vacuo* to yield a light yellow solid.

$(Cz^{tBu}(Pyr^{H})_2)_2Zn$ (1). Yield: 91%. Crystals suitable for X-ray diffraction were grown from slow evaporation of a DCM solution at ambient temperature. ^1H NMR (500 MHz, C_6D_6, δ): 8.67 (s, 2H, Ar*H*), 7.42 (s, 2H, Ar*H*), 6.81 (s, 2H, Ar*H*), 5.34 (s, 2H, Ar*H*), 1.52 (s, 18H, $C(CH_3)_3$). UV−vis (acetonitrile, 22 °C) λ_{max} (ε [$M^{-1}\cdot cm^{-1}$]): 214 (176582), 255 (46257), 261 (46386), 268 (31756), 315 (19421). Anal. Calcd for $(Cz^{tBu}(Pyr^{H})_2)_2Zn$: C, 70.46; H, 6.37; N, 15.80. Found: C, 70.06; H, 6.36; N, 15.86.

$(Cz^{tBu}(Pyr^{Me})_2)_2Zn$ (2). Yield: 62%. Crystals suitable for X-ray diffraction were grown from a concentrated toluene solution at ambient temperature. ^1H NMR (500 MHz, C_6D_6, δ): 8.52 (s, 2H, Ar*H*), 7.74 (s, 2H, Ar*H*), 7.47 (s, 2H, Ar*H*), 5.27 (s, 2H, Ar*H*), 1.46 (s, 18H, $C(CH_3)_3$), 1.36 (s, 6H, CH_3). UV−vis (acetonitrile, 23 °C) λ_{max} (ε [$M^{-1}\cdot cm^{-1}$]): 208 (64090), 243 (26070), 313 (11960). Anal. Calcd for $(Cz^{tBu}(Pyr^{Me})_2)_2Zn$: C, 71.36; H, 6.84; N, 14.86. Found: C, 70.97; H, 6.90; N, 14.60.

$(Cz^{tBu}(Pyr^{iPr})_2)_2Zn$ (3). Yield: 86%. Crystals suitable for X-ray diffraction were grown from slow diffusion of *n*-pentane into a THF solution at ambient temperature. ^1H NMR (500 MHz, C_6D_6, δ): 8.50 (s, 2H, Ar*H*), 7.79 (s, 2H, Ar*H*), 7.49 (s, 2H, Ar*H*), 5.49 (s, 2H, Ar*H*), 2.31 (m, J = 2.0 Hz, 2H, $CH(CH_3)_2$), 1.44 (s, 18H, $C(CH_3)_3$), 0.66 (d, J = 2.0 Hz, 12H, $CH(CH_3)_2$). UV−vis (acetonitrile, 23 °C) λ_{max} (ε [$M^{-1}\cdot cm^{-1}$]): 209 (76970), 243 (26840), 312 (12640). Anal. Calcd for $(Cz^{tBu}(Pyr^{iPr})_2)_2Zn$: C, 72.88; H, 7.65; N, 13.28. Found: C, 72.61; H, 7.40; N, 13.66.

Crystallography. Data for **1** was measured using a Bruker Kappa APEXII diffractometer with Mo Kα radiation (λ = 0.71073 Å). Data for **2** and **3** were collected using a Bruker AXS D8 Quest diffractometer with a PhotonII charge-integrating pixel array detector (CPAD) with Mo Kα radiation (λ = 0.71073 Å). A single crystal of each compound was mounted on a MiTeGen micromesh mount using a trace of mineral oil and cooled *in situ* to 120 or 150 K for data collection. Data for **1**, **2**, and **3** was collected using an Apex2 or Apex3,[17,18] and the intensity data were corrected for absorption using multiscan techniques (SADABS).[19] The space groups were assigned, and the structures were solved by direct methods using XPREP within the SHELXTL suite of programs and refined by full matrix least squares against F^2 with all reflections using Shelxl2014 or 2018 using the graphical interface Shelxle or OLEX2.[17,20,21] H atoms attached to carbon atoms were positioned geometrically and constrained to ride on their parent atoms, with carbon hydrogen bond distances of 0.95 Å for alkene and aromatic C−H, and 1.00, 0.99, and 0.98 Å for aliphatic CH, CH_2, and CH_3 moieties, respectively. Methyl H atoms were allowed to rotate but not to tip to best fit the experimental electron density. U_{iso}(H) values were set to a multiple of U_{eq}(C) with 1.5 for CH_3 and 1.2 for CH_2 and CH units. Additional experimental details for all structures are given in the Supporting Information. Structures, in CIF format, have been deposited with the Cambridge Crystallographic Data Centre, CCDC 2182333−2182335. These data can be obtained free of charge from The Cambridge Crystallographic Data Centre via https://www.ccdc.cam.ac.uk/structures/.

Molecular Dynamics (MD) Simulations. MD simulations were performed by using the general AMBER force field (GAFF).[22] Any missing parameters for the metal sites were generated using the MCPB.py program.[23] For each of Compounds **2** and **3**, one of the pyrazole moieties was flipped to allow the compound to chelate with the metal ion. A 1 μs production simulation was performed for each of the two compounds in acetonitrile and in water. Further details of the simulations are provided in the Supporting Information. This work utilized the computational resources of the Extreme Science and Engineering Discovery Environment (XSEDE).[38]

RESULTS AND DISCUSSION

Compounds **1**−**3** were synthesized according to Scheme 1. Briefly, deprotonation of $HCz^{tBu}(Pyr^{R})_2$ (R = H, Me, ^{i}Pr) followed by transmetallation with $ZnCl_2$ afforded **1**−**3** in good yields. All complexes were characterized using ^1H NMR

Scheme 1. Synthesis of 1−3

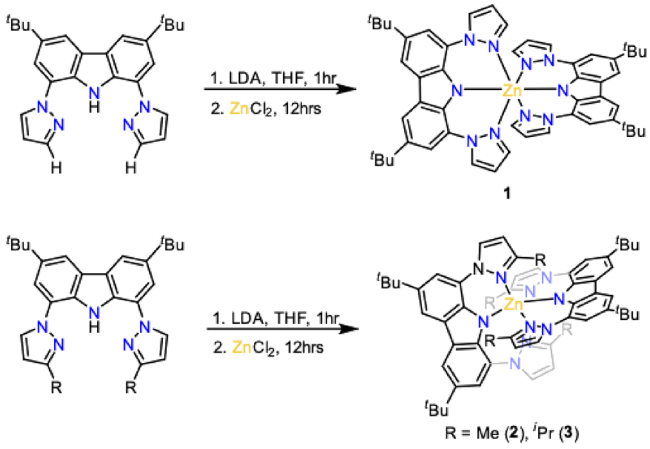

https://doi.org/10.1021/acsomega.2c06058
ACS Omega 2023, 8, 3835−3841

spectroscopy, elemental analysis, single-crystal X-ray diffraction, UV−vis spectroscopy, and spectrofluorometry. Crystal data collection and refinement details are summarized in Table S1. An ORTEP diagram of **3** is shown in Figure 1, and ORTEP

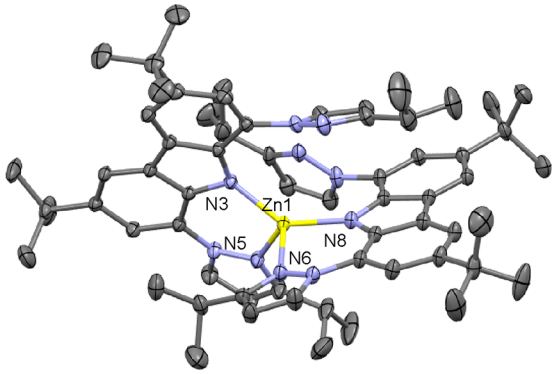

Figure 1. Molecular structure of **3** with thermal ellipsoids at the 50% probability level. Hydrogen atoms and solvent molecules are omitted for clarity. Color key: yellow = Zn, blue = N, gray = C.

diagrams of **1** and **2** are shown in Figures S1 and S2. The Zn^{2+} metal center resides in a distorted octahedral geometry in compound **1**. Interestingly, **2** resides in a distorted tetrahedral environment best described as a seesaw geometry (τ_4 = 0.75, τ_4' = 0.64) with N3−Zn1−N8 and N3−Zn1−N6 bond angles of 145.30° and 108.03°, respectively.[24,25] The Zn^{2+} center is coordinated by two $Cz^{tBu}(Pyr^{Me})_2^-$ ligands in a κ^2 coordination fashion, with one pyrazole moiety from each ligand remaining uncoordinated. The preference for a seesaw geometry, as opposed to an octahedral geometry observed in **1**, is believed to be caused by increased steric hindrance due to the methyl group substitution on the pyrazole rings. In a similar fashion to **2**, **3** also resides in a distorted tetrahedral geometry (τ_4 = 0.78, τ_4' = 0.64) with N3−Zn1−N8 and N3−Zn1−N6 bond angles of 137.00° and 116.19°, respectively, and one uncoordinated pyrazole moiety from each ligand.

UV−vis spectra of **1**−**3** in acetonitrile (MeCN) are shown in Figure S3. Complex **1** displays an absorption maximum peak ($\lambda_{max,abs}$) at 404 nm, and both complex **2** and **3** exhibit $\lambda_{max,abs}$ at 374 nm. The UV−vis spectra of **2** and **3** are practically identical, whereas **1** is different. This suggests that **2** and **3** do indeed retain a distorted tetrahedral geometry in solution, as opposed to rapid interconversion between 4- and 6-coordinate environments. Complex **1** has a maximum emission peak ($\lambda_{max,\ em}$) at 426 nm (Figure S4). Complex **2** exhibits $\lambda_{max,em}$ at 410 nm (Figure S5). Complex **3** displays $\lambda_{max,em}$ at 421 nm (Figure 2).

The ability of **1**−**3** to selectively detect cations was then studied by recording the emission spectra of each complex with varying amounts of biologically relevant cations (Ca^{2+}, Mg^{2+}, K^+, Na^+, Zn^{2+}) as well as Cd^{2+}. A moderate decrease in fluorescence intensity was noted for **1** in the presence of all cations tested (Figure S4). Conversely, **2** responded to cations with a shift in $\lambda_{max,em}$ to 387 nm as well as a significant increase in fluorescence intensity (*ca.* 6-fold), albeit unselectively (Figure S5). Complex **3**, however, exhibited a similar peak shift to 387 nm and increased fluorescence in the presence of Mg^{2+} with high selectivity and little to no response in the presence of Ca^{2+}, Na^+, K^+ (Figure 2). Current Mg^{2+} probes often have selectivity issues with cadmium and zinc ions, though for imaging purposes, this does not pose a significant problem.[6] **3** did exhibit a moderate increase in emission intensity in the presence of Cd^{2+} and Zn^{2+} (Figure S6). However, Cd^{2+} is not present in healthy cells, and Zn^{2+} concentrations inside eukaryotic cells are drastically lower than that of Mg^{2+} (fM vs mM, respectively) as well as 100-times lower intracellularly.[26−28]

To ensure that all changes in fluorescence were due to metal complex **3** as opposed to the dissociated free ligand, the emission spectra of $HCz^{tBu}(Pyr^{iPr})_2$ (Figure S7) and $Cz^{tBu}(Pyr^{iPr})_2^-$ (Figure S8) were measured. Both emission spectra intensities vary greatly from that of **3** and exhibit a slight decrease in intensity in the presence of Mg^{2+}, thus confirming that only **3** acts as the fluorescent probe. The fact that the ligand backbone only displays favorable interaction with Mg^{2+} when it is complexed to Zn^{2+} further supports the use of inorganic scaffolding for fluorescent chemosensors.

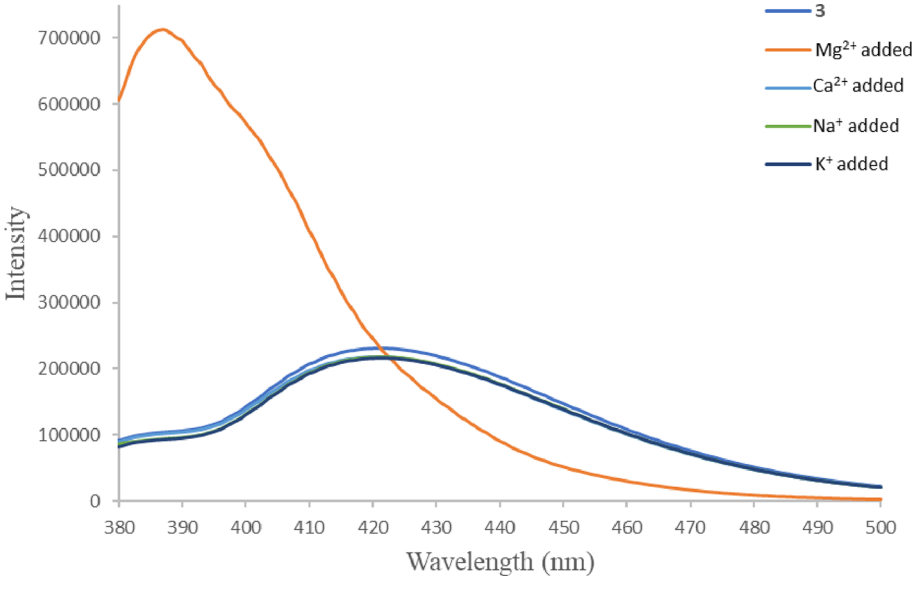

Figure 2. Fluorescence emission spectra of 5 μM **3** in acetonitrile at 22 °C, alone, and in the presence of cations (1 equiv of each cation added).

https://doi.org/10.1021/acsomega.2c06058
ACS Omega 2023, 8, 3835−3841

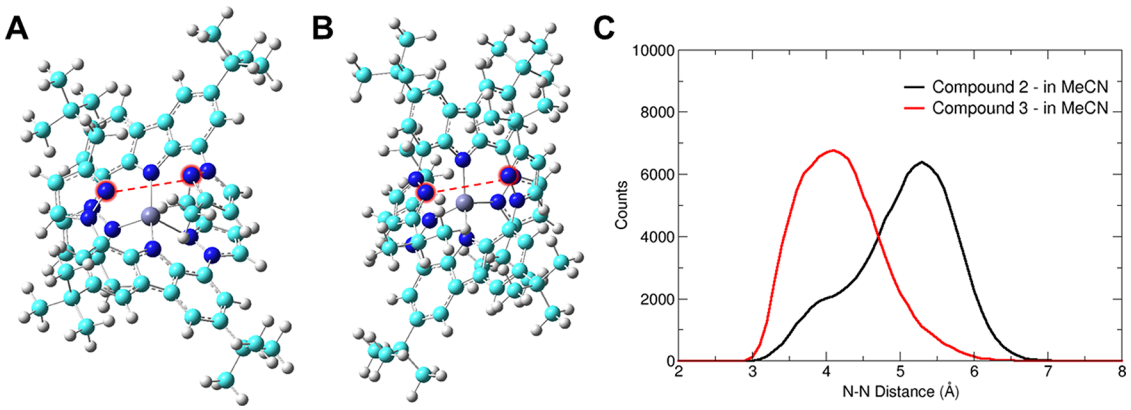

Figure 3. Illustration of the distance between the two chelating N atoms (in red circles) in the NNN pincer ligands in (A) **2** or (B) **3** along with (C) the distance distributions obtained from the MD simulations of these two compounds. Binsize was set as 0.1 Å for generating the histograms.

A plot of fluorescence intensity reveals a linear range of detection from 0.27 to 0.8 equiv of Mg^{2+} (Figure S9). Additionally, the result suggests that the magnesium ion interacts with **3** in a 1:1 fashion. The dissociation constant (K_d) of Mg^{2+} with **3** was determined using a previously reported method in which K_d is found as the x intercept on a plot of $-\log[\beta(R - R_{min}/R_{max} - R)]$ as a function of $-\log[Mg^{2+}]$.[29] Here, β represents the ratio of minimum and maximum emission at the shifted emission peak (387 λ_{min}/387 λ_{max}), R_{min} is the ratio of emission peaks with no Mg^{2+} present, R_{max} is the ratio determined when **3** is saturated with Mg^{2+}, and R is the ratio of emission wavelengths at some point in the linear range of detection.[29] The double log plot (Figure S10) gives a mean K_d value of 3.62 μM. An alternative method, the Benesi−Hildebrand linear regression analysis, gave an averaged K_d value of 7.41 μM over three trials within the linear range of detection.[30] Due to its incorporation of the change in $\lambda_{max,em}$, it is believed that the first method of determination is more accurate. Overall, both methods support a K_d in the micromolar range, which is significantly lower than most available Mg^{2+} sensors and is an encouraging sign for the use of **3** as a fluorescent probe.[6]

Analysis of the crystal structures of **1**−**3** provided us with a working hypothesis as to why **3** is able to interact with magnesium ions selectively. Complex **1**, with fully coordinated pyrazole moieties, fails to display increased fluorescence in the presence of any metal ion, whereas tetrahedral complexes **2** and **3** do. This suggests that the uncoordinated pyrazole arms of **2** and **3** act as the binding site. We believe that the difference in steric effects between the methyl and isopropyl groups of **2** and **3** may correspond to the cavity size between the uncoordinated pyrazole side arms. This cavity size could relate to the size of the ions with which **2** and **3** are capable of interacting via a "snug-fit" model. To gain further insight into the validity of this hypothesis, we performed microsecond molecular dynamics (MD) simulations for **2** and **3**. We calculated the angle between the two chelating pyrazole moieties, defined as the angle between the two C−N vectors in the uncoordinated rings (Figure S14). The distributions for **2** and **3** are Gaussian-shaped with a relatively large width, indicating that both compounds are flexible for chelation to a secondary analyte. However, we found that the distributions for **2** and **3** are slightly different: **3** has a slightly more dispersed distribution than **2** while it also showed a smaller equilibrium angle. These subtle differences may imply that **2** and **3** have different abilities to selectively bind to metal ions.

Unlike the angle distribution, the distance distribution differentiates the two compounds significantly (Figure 3). For **2**, the N−N distance distribution has a peak centered at ∼5.3 Å. In comparison, the N−N distance distribution of **3** has a peak centered at ∼4.1 Å. The two nitrogen atoms have lone pairs that repel each other. This shorter N−N distance in **3** may be attributable to the greater steric hindrance of the isopropyl groups preventing the two nitrogen atoms from getting too far away when compared to the less bulky methyl groups in **2**. The difference of the N−N distance distributions between **2** and **3** may explain their different selectivity when coordinating with different metal ions. Specifically, the N−N distance of **3** is in much better agreement with the sizes of Mg^{2+} and Zn^{2+}. Indeed, according to crystal structures, the average distance between Zn^{2+} and ligating nitrogen atoms is 2.20 Å when coordinated with six imidazole groups.[31] Similarly, the average distance between Mg^{2+} and ligating nitrogen atoms is 2.18 Å when it coordinates with three imidazole groups and three water molecules.[32] In comparison, Cd^{2+} showed a significantly larger ion size. For example, it resides with an ion−nitrogen distance of 2.36 Å when it coordinates with six imidazole groups.[33] We have also analyzed the distances between Ca^{2+} and the imidazole nitrogen atoms for the Ca^{2+}−histidine coordination bonds based on the structures, which have resolution within 2 Å in the MESPEUS database (version 2019).[34,35] We find the averaged distance is 2.50 Å, which is larger than the Cd^{2+}−nitrogen distance as mentioned above. Such a size pattern can also be seen in the aqueous solution, where both Mg^{2+} and Zn^{2+} exhibit an ion−oxygen distance of 2.09 Å, while Cd^{2+} exhibits an ion−oxygen distance of 2.30 Å in aqueous solution.[36] In contrast, Ca^{2+} has an ion−oxygen distance of 2.46 Å in aqueous solution,[37] which is also larger than that of Cd^{2+}. Given that previous studies have shown that ion size is important for ion selectivity,[7] the above results imply that complex **3** interacts stronger with Mg^{2+} and Zn^{2+} than with Cd^{2+}, which is consistent with the observed experimental data (Figure S6). In contrast, the longer N−N distance of **2** (∼5.3 Å) is similarly large for Mg^{2+}, Zn^{2+}, and Cd^{2+}, agreeing with the observed fluorescence emissions of **2** (Figure S5). In general, we believe that these MD simulations provide molecular insights into the ability of **2** and **3** to interact with ions in solutions. Furthermore, these results support our hypothesis that selective interaction

https://doi.org/10.1021/acsomega.2c06058
ACS Omega 2023, 8, 3835−3841

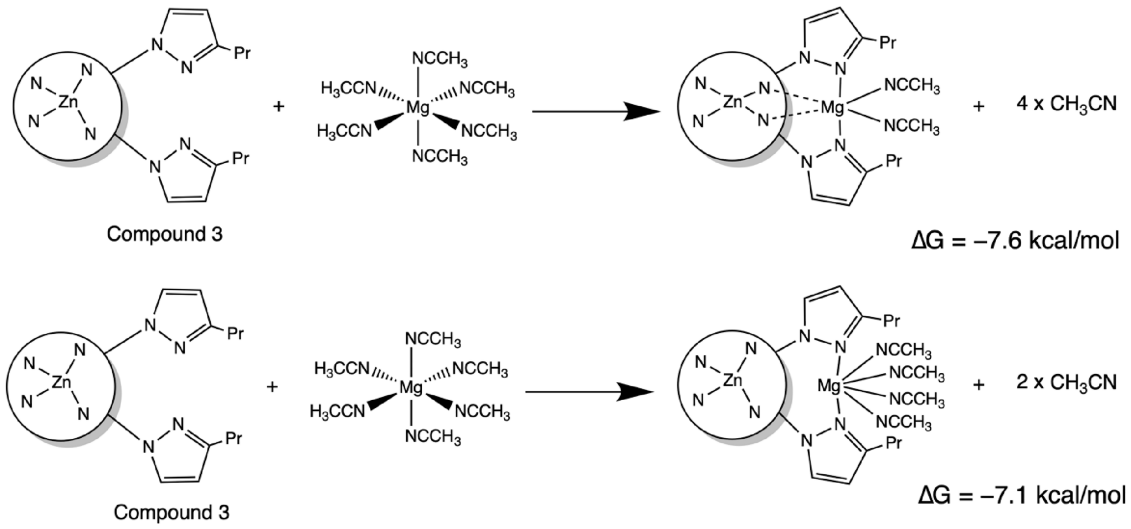

Figure 4. QM calculations to characterize the structure of Mg^{2+}-coordinated **3**. Herein, both Zn and Mg are divalent.

between Mg^{2+} and **3** occurs as a result of well-controlled cavity size formation between the uncoordinated pyrazole arms.

To further characterize the structure of Mg^{2+}-coordinated **3**, we performed additional QM calculations (Figure 4). The B3LYP-D3/6-311G* level of theory was used with the PCM implicit solvent model to mimic the acetonitrile solvent. For each compound, geometry was optimized and frequency analysis was performed to confirm the stationary point. Moreover, the following correction was applied to calculate the free energy of each compound in the liquid phase ($G_{1M} = G_{1atm} + RT \ln C$, with $RT \ln C = 1.9$ kcal/mol). Herein, G represents the Gibbs free energy, R is the gas constant, T is the temperature, which is 298.15 K, and C is the volume ratio V_{1atm}/V_{1M} when 1 mol gas (24.5 L) was dissolved in 1 L water to yield 1 mol/L solution at 298.15 K and 1 atm. The results show that the structure with Mg^{2+} coordinated to two acetonitriles has comparable free energy to that of the structure with Mg^{2+} coordinated to four acetonitriles, implying that both structures are populated at room temperature. Intriguingly, Mg^{2+} is 6-coordinated in both structures but with different modes: in the former structure, two nitrogen atoms act as bridging atoms, which coordinate to both Zn^{2+} and Mg^{2+}, with their distances to Mg^{2+} both as 2.36 Å. In contrast, in the latter structure, these two nitrogen atoms do not coordinate to Mg^{2+}, with their distances to Mg^{2+} becoming larger than 4 Å. The optimized geometries of the compounds are shown in the SI.

Given the potential biological applications of analogous complexes, we performed microsecond MD simulations for **2** and **3** in water to learn more about whether ion selectivity would remain. The simulation details and the results are provided in the SI. Interestingly, different results to those recorded in acetonitrile were obtained in water. In particular, **2** and **3** show similar angle distributions between the C−N vectors (Figure S15) and also similar N−N distance distributions (Figure S16). Specifically, the most probable N−N distances are ∼4.5 Å for **2** and ∼4.3 Å for **3**. Both of these two distances agree well with the size of Mg^{2+} (see discussion above). These results imply that ion selectivity might be conserved for **3** in water, while the selectivity might be enhanced more for **2** in water than it is in acetonitrile.

CONCLUSIONS

We have designed a fluorescent probe, **3**, that displays greatly increased fluorescence in the presence of Mg^{2+}. A review of the available literature suggests that this is the first Zn-based probe developed for the detection of cations, and our results indicate that further development of inorganic fluorescent chemosensors may be warranted. We hypothesize that the key advantage displayed herein is the ability to fine tune the 3D geometric parameters at the pyrazole moiety binding site, with remarkable changes in selectivity based on steric effect. This hypothesis is supported by microsecond MD simulations, which suggest that **3** displays an optimal N−N distance between the uncoordinated pyrazole rings for coordination to Mg^{2+} ions. Future work will include modifying the ligand scaffolding such that the resulting Zn^{2+} complexes emit at higher wavelengths and are more water soluble. Additionally, other, more redox active metal centers may be tested to study the effect that metal oxidation state has on ion selectivity.

ASSOCIATED CONTENT

Supporting Information

The Supporting Information is available free of charge at https://pubs.acs.org/doi/10.1021/acsomega.2c06058.

Spectroscopy data, NMR spectra, and computational details (PDF)

Crystallographic data of **3** (CIF)

Crystallographic data of **2** (CIF)

Crystallographic data of **1** (CIF)

AUTHOR INFORMATION

Corresponding Authors

Pengfei Li − *Department of Chemistry and Biochemistry, Loyola University Chicago, Chicago, Illinois 60660, United States;* orcid.org/0000-0002-2572-5935; Email: pli4@luc.edu

Wei-Tsung Lee − *Department of Chemistry and Biochemistry, Loyola University Chicago, Chicago, Illinois 60660, United States;* orcid.org/0000-0002-2198-3398; Email: wlee5@luc.edu

https://doi.org/10.1021/acsomega.2c06058
ACS Omega 2023, 8, 3835−3841

Authors

Theodore Gerard − *Department of Chemistry and Biochemistry, Loyola University Chicago, Chicago, Illinois 60660, United States*

Yang Wei − *Department of Chemistry and Biochemistry, Loyola University Chicago, Chicago, Illinois 60660, United States*

Erwin Weerawardhana − *Department of Chemistry and Biochemistry, Loyola University Chicago, Chicago, Illinois 60660, United States*

Adriana Lugosan − *Department of Chemistry and Biochemistry, Loyola University Chicago, Chicago, Illinois 60660, United States*

Matthias Zeller − *Department of Chemistry, Purdue University, West Lafayette, Indiana 47907, United States;* orcid.org/0000-0002-3305-852X

Diane A. Dickie − *Department of Chemistry, Brandeis University, Waltham, Massachusetts 02453, United States;* Present Address: Department of Chemistry, University of Virginia, Charlottesville, Virginia 22904, United States (D.A.D.); orcid.org/0000-0003-0939-3309

Complete contact information is available at: https://pubs.acs.org/10.1021/acsomega.2c06058

Notes

The authors declare no competing financial interest.

■ ACKNOWLEDGMENTS

This work was funded by start-up funds from Loyola University Chicago (to W.-T.L. and P.L.). P.L. acknowledges the computational support from the Extreme Science and Engineering Discovery Environment (XSEDE), which is funded by the National Science Foundation (NSF) with Grant Number ACI-1548562. Specifically, this work utilized the CPU and GPU resources on Expanse at the San Diego Supercomputing Center (Allocation Number: TG-BIO210105).

■ REFERENCES

(1) Czarnik, A. W. *Fluorescent Chemosensors for Ion and Molecule Recognition*, American Chemical Society: Washington, DC, 1993, DOI: 10.1021/bk-1993-0538.

(2) (a) Parmar, B.; Rachuri, Y.; Bisht, K. K.; Laiya, R.; Suresh, E. Mechanochemical and Conventional Synthesis of Zn(II)/Cd(II) Luminescent Coordination Polymers: Dual Sensing Probe for Selective Detection of Chromate Anions and TNP in Aqueous Phase. *Inorg. Chem.* **2017**, *56*, 2627−2638. (b) Rachuri, Y.; Parmar, B.; Bisht, K. K.; Suresh, E. Mixed ligand two dimensional Cd(II)/Ni(II) metal organic frameworks containing dicarboxylate and tripodal N-donor ligands: Cd(II) MOF is an efficient luminescent sensor for detection of picric acid in aqueous media. *Dalton Trans.* **2016**, *45*, 7881−7892. (c) Rachuri, Y.; Parmar, B.; Suresh, E. Three-Dimensional Co(II)/Cd(II) Metal-Organic Frameworks: Luminescent Cd-MOF for Detection and Adsorption of 2,4,6-Trinitrophenol in Aqueous Phase. *Cryst. Growth Des.* **2018**, *18*, 3062−3072. (d) Zhu, X. D.; Zhang, K.; Wang, Y.; Long, W. W.; Sa, R. J.; Liu, T. F.; Lu, J. Fluorescent Metal-Organic Framework (MOF) as a Highly Sensitive and Quickly Responsive Chemical Sensor for the Detection of Antibiotics in Simulated Wastewater. *Inorg. Chem.* **2018**, *57*, 1060−1065.

(3) Wu, D.; Sedgwick, A. C.; Gunnlaugsson, T.; Akkaya, E. U.; Yoon, J.; James, T. D. Fluorescent chemosensors: the past, present, and future. *Chem. Soc. Rev.* **2017**, *46*, 7105−7123.

(4) Kwon, N.; Hu, Y.; Yoon, J. Fluorescent Chemosensors for Various Analytes Including Reactive Oxygen Species, Biothiol, Metal Ions, and Toxic Gases. *ACS Omega* **2018**, *3*, 13731−13751.

(5) Formica, M.; Fusi, V.; Giorgi, L.; Micheloni, M. New fluorescent chemosensors for metal ions in solution. *Coord. Chem. Rev.* **2012**, *256*, 170−192.

(6) Liu, M.; Yu, X.; Li, M.; Liao, N.; Bi, A.; Jiang, Y.; Liu, S.; Gong, Z.; Zeng, W. Fluorescent probes for the detection of magnesium ion (Mg^{2+}): from design to application. *RSC Adv.* **2018**, *8*, 12573−12587.

(7) Dudev, T.; Lim, C. Competition among metal ions for protein binding sites: determinants of metal ion selectivity in proteins. *Chem. Rev.* **2014**, *114*, 538−556.

(8) Cheng, J.; Zhou, X.; Xiang, H. Fluorescent metal ion chemosensors via cation exchange reactions of complexes, quantum dots, and metal-organic frameworks. *Analyst* **2015**, *140*, 7082−7115.

(9) Komatsu, H.; Iwasawa, N.; Citterio, D.; Suzuki, Y.; Kubota, T.; Tokuno, K.; Kitamura, Y.; Oka, K.; Suzuki, K. Design and synthesis of highly sensitive and selective fluorescein-derived magnesium fluorescent probes and application to intracellular 3D Mg^{2+} imaging. *J. Am. Chem. Soc.* **2004**, *126*, 16353−16360.

(10) Gout, E.; Rebeille, F.; Douce, R.; Bligny, R. Interplay of Mg^{2+}, ADP, and ATP in the cytosol and mitochondria: Unravelling the role of Mg^{2+} in cell respiration. *PNAS* **2014**, *111*, 4560−4567.

(11) Swaminathan, R. Magnesium metabolism and its disorders. *Clin. Biochem. Rev.* **2003**, *24*, 47−66.

(12) Farruggia, G.; Iotti, S.; Prodi, L.; Montalti, M.; Zaccheroni, N.; Savage, P. B.; Trapani, V.; Sale, P.; Wolf, F. I. 8-Hydroxyquinoline Derivatives as Fluorescent Sensors for Magnesium in Living Cells. *J. Am. Chem. Soc.* **2005**, *128*, 344−350.

(13) Azadbakht, R.; Koolivand, M.; Menati, S. Salicylimine-based fluorescent chemosensor for magnesium ions in aqueous solution. *Inorg. Chim. Acta* **2021**, *514*, 1−8.

(14) Jing, Z.; Liu, C.; Qi, R.; Ren, P. Many-body effect determines the selectivity for Ca^{2+} and Mg^{2+} in proteins. *PNAS* **2018**, *115*, 7495−7501.

(15) Berg, J. Zinc fingers and other metal-binding domains. Elements for interactions between macromolecules. *Receptor* **1990**, *265*, 6513−6516.

(16) Ghannam, J.; Al Assil, T.; Pankratz, T. C.; Lord, R. L.; Zeller, M.; Lee, W.-T. A Series of 4- and 5-Coordinate Ni(II) complexes. *Inorg. Chem.* **2018**, *57*, 8307−8316.

(17) Hübschle, C. B.; Sheldrick, G. M.; Dittrich, B. ShelXle: a Qt graphical user interface for SHELXL. *J. Appl. Crystallogr.* **2011**, *44*, 1281−1284.

(18) *Apex2 v2013.4−1, v2014.11, v2014.1−1, Apex3 v2019.11−0, SAINT V8.34A, SAINT V8.30C, V8.40B*, Bruker AXS Inc.: Madison(WI), USA, 2013/2014.

(19) Blessing, R. An empirical correction for absorption anisotropy. *Acta Crystallogr., Sect. A: Found. Crystallogr.* **1995**, *51*, 33−38.

(20) Dolomanov, O. V.; Bourhis, L. J.; Gildea, R. J.; Howard, J. A. K.; Puschmann, H. OLEX2: a complete structure solution, refinement and analysis program. *J. Appl. Crystallogr.* **2009**, *42*, 339−341.

(21) Sheldrick, G. A short History of SHELX. *Acta Crystallogr., Sect. A: Found. Crystallogr.* **2008**, *64*, 112−122.

(22) Wang, J.; Wolf, R. M.; Caldwell, J. W.; Kollman, P. A.; Case, D. A. Development and testing of a general amber force field. *J. Comput. Chem.* **2004**, *25*, 1157−1174.

(23) Li, P.; Merz, K. M. MCPB.py: A Python Based Metal Center Parameter Builder. *J. Chem. Inf. Model.* **2016**, *56*, 599−604.

(24) Yang, L.; Powell, D.; Houser, R. Structural variation in copper(I) complexes with pyridylmethylamide ligands: structural analysis with a new four-coordinate geometry index, τ_4. *Dalton Trans.* **2007**, *9*, 955−964.

(25) Okuniewski, A.; Rosiak, D.; Chojnacki, J.; Becker, B. Coordination polymers and molecular structures among complexes of mercury(II) halides with selected 1-benzoylthioureas. *Polyhedron* **2015**, *90*, 47−57.

(26) Dudev, T.; Lim, C. Metal Selectivity in Metalloproteins: Zn^{2+} vs Mg^{2+}. *J. Phys. Chem. B* **2001**, *105*, 446−452.

(27) Williams, R. J. P.; Fraústo Da Silva, J. J. R. The distribution of elements in cells. *Coord. Chem. Rev.* **2000**, *200*, 247−348.
(28) Suhy, D. A.; Simon, K. D.; Linzer, D. I. H.; O'Halloran, T. V. Metallothionein is Part of a Zinc-scavenging Mechanism for Cell Survival under Conditions of Extreme Zinc Deprivation. *J. Biol. Chem.* **1999**, *274*, 9183−9192.
(29) Petr, M. J.; Wurster, R. D. Determination of *in situ* dissociation constant for Fura-2 and quantitation of background fluorescence in astrocyte cell line U373-MG. *Cell Calcium* **1997**, *21*, 233−240.
(30) Mukhopadhyay, M.; Banerjee, D.; Koll, A.; Mandal, A.; Filarowski, A.; Fitzmaurice, D.; Das, R.; Mukherjee, S. Excited state intermolecular proton transfer and caging of salicylidine-3,4,7-methyl amine in cyclodextrins. *J. Photochem. Photobiol., A* **2005**, *175*, 94−99.
(31) Sandmark, C.; Brändén, C. I.; Kjekshus, A.; Åkeson, Å.; Theorell, H.; Blinc, R.; Paušak, S.; Ehrenberg, L.; Dumanović, J. The Crystal Structure of Hexaimidazole Zinc(II) Dichloride Tetrahydrate, $Zn(C_3H_4N_2)_6Cl_2 \cdot 4\ H_2O$. *Acta Chem. Scand.* **1967**, *21*, 993−999.
(32) Unger, Y.; Taige, M. A.; Ahrens, S.; Strassner, T. Synthesis and solid-state structure of magnesium and calcium imidazole complexes. *Inorg. Chim. Acta* **2007**, *360*, 3699−3704.
(33) Mighell, A. D.; Santoro, A. The Crystal and Molecular Structures of Hexakis(imidazole)cadmium(II) Nitrate, $[Cd(C_3H_4N_2)_6](NO_3)_2$, and Hexakis(imidazole)cadmium(II) Hydroxide Nitrate Tetrahydrate, $[Cd(C_3H_4N_2)_6](OH)(NO_3) \cdot 4\ H_2O$. *Acta Crystallogr., Sect. B: Struct. Crystallogr. Cryst. Chem.* **1971**, *27*, 2089−2097.
(34) Hsin, K.; Sheng, Y.; Harding, M. M.; Taylor, P.; Walkinshaw, M. D. MESPEUS: a database of the geometry of metal sites in proteins. *J. Appl. Crystallogr.* **2008**, *41*, 963−968.
(35) Harding, M. M.; Hsin, K. Mespeus - A Database of Metal Interactions with Proteins. In *Structural Genomics. Methods in Molecular Biology*, Vol. 1091; Chen, Y., Ed.; Humana Press, 2014; 333−342.
(36) Marcus, Y. Ionic radii in aqueous solutions. *Chem. Rev.* **1988**, *88*, 1475−1498.
(37) Jalilehvand, F.; Spangberg, D.; Lindqvist-Reis, P.; Hermansson, K.; Persson, I.; Sandstrom, M. Hydration of the Calcium Ion. An EXAFS, Large-Angle X-ray Scattering, and Molecular Dynamics Simulation Study. *J. Am. Chem. Soc.* **2001**, *123*, 431−441.
(38) Towns, J.; Cockerill, T.; Dahan, M.; Foster, I.; Gaither, K.; Grimshaw, A.; Hazlewood, V.; Lathrop, S.; Lifka, D.; Peterson, G. D.; Roskies, R.; Scott, J. R.; Wilkins-Diehr, N. XSEDE: Accelerating Scientific Discovery. *Comput. Sci. Eng.* **2014**, *16*, 62−74.

https://doi.org/10.1021/acsomega.2c06058
ACS Omega 2023, 8, 3835−3841